



OPEN

SUBJECT AREAS:
BATTERIES
SPECTROSCOPYReceived
27 December 2013Accepted
16 June 2014Published
16 July 2014Correspondence and
requests for materials
should be addressed to
F.L. (flin@lbl.gov) or
H.L.X. (hxin@bnl.gov)

Chemical and Structural Stability of Lithium-Ion Battery Electrode Materials under Electron Beam

Feng Lin¹, Isaac M. Markus^{1,2}, Marca M. Doeff¹ & Huolin L. Xin³¹Environmental Energy Technologies Division, Lawrence Berkeley National Laboratory, Berkeley, CA 94720, USA, ²Department of Materials Science and Engineering, University of California, Berkeley, CA 94720, USA, ³Center for Functional Nanomaterials, Brookhaven National Laboratory, Upton, NY 11973, USA.

The investigation of chemical and structural dynamics in battery materials is essential to elucidation of structure-property relationships for rational design of advanced battery materials. Spatially resolved techniques, such as scanning/transmission electron microscopy (S/TEM), are widely applied to address this challenge. However, battery materials are susceptible to electron beam damage, complicating the data interpretation. In this study, we demonstrate that, under electron beam irradiation, the surface and bulk of battery materials undergo chemical and structural evolution equivalent to that observed during charge-discharge cycling. In a lithiated NiO nanosheet, a Li₂CO₃-containing surface reaction layer (SRL) was gradually decomposed during electron energy loss spectroscopy (EELS) acquisition. For cycled LiNi_{0.4}Mn_{0.4}Co_{0.18}Ti_{0.02}O₂ particles, repeated electron beam irradiation induced a phase transition from an R $\bar{3}m$ layered structure to an Fm $\bar{3}m$ rock-salt structure, which is attributed to the stoichiometric lithium and oxygen removal from R $\bar{3}m$ 3a and 6c sites, respectively. Nevertheless, it is still feasible to preserve pristine chemical environments by minimizing electron beam damage, for example, using fast electron imaging and spectroscopy. Finally, the present study provides examples of electron beam damage on lithium-ion battery materials and suggests that special attention is necessary to prevent misinterpretation of experimental results.

Lithium-ion batteries are used in a variety of consumer electronics, such as mobile phones, tablets and laptops, and are now being commercialized for use in electric vehicles (EVs) and plug-in hybrid electric vehicles (PHEVs)^{1–4}. In order to achieve reliable battery packs for these applications, various thrusts of research and development must be conducted simultaneously, including but not limited to the design of advanced battery materials, cell configuration, circuit optimization, and diagnostics. With respect to the chemistries of electrode materials, various analytical diagnostic tools have been performed to probe chemical and structural environments from the bulk to the surface^{5–9}. In-depth diagnostic analysis can provide insights into structure-property relationships^{10,11} as well as into failure mechanisms^{12,13}. In combination with many ensemble-averaged measurements, fast electron microscopy and spectroscopy are poised to reveal chemical and structural information with extremely high spatial resolution and potentially improved temporal resolution through *in situ* transmission electron microscopy (TEM) visualization^{14,15}. To date, a vast number of studies have been successfully implemented by virtue of the state-of-the-art imaging and spectroscopy capabilities of fast electron microscopy.

The chemical environment at the particle surface determines the way an active electrode interacts with its surrounding electrolyte and impacts the resulting cycling behaviors. Surface modifications, such as artificial solid-electrode interphases, were reported to improve cycling performance^{16,17}. On the other hand, electrochemistry-induced surface reaction layers (SRLs), such as solid-electrolyte interphases at anode material particle surfaces, also play critical roles in determining the way electrode materials interact with electrolytic solutions and how lithium ions intercalate¹⁸. SRLs are generally composed of oligomers and inorganic compounds that are formed from the electrochemical reduction of solvent and electrolytic salt¹⁹. Similar to the behavior of many organic compounds under electron beams, SRLs are prone to beam damage. Structural changes may also occur as a result of charge-discharge cycling, and have been proven to impact battery performance. For example, in LiNi_xMn_xCo_{1–2x}O₂ (NMC), lithium-rich Li(Li_yNi_{x–y}Mn_xCo_{1–2x})O₂, lithium-rich/manganese-rich xLi₂MnO₃·(1–x)LiMO₂ (M = Mn, Ni, Co, etc.) materials, the transition from layered structures to spinel and/or rock-salt structures leads to impedance buildup, voltage decay, and capacity fading^{5,12,20,21}. The referenced studies were

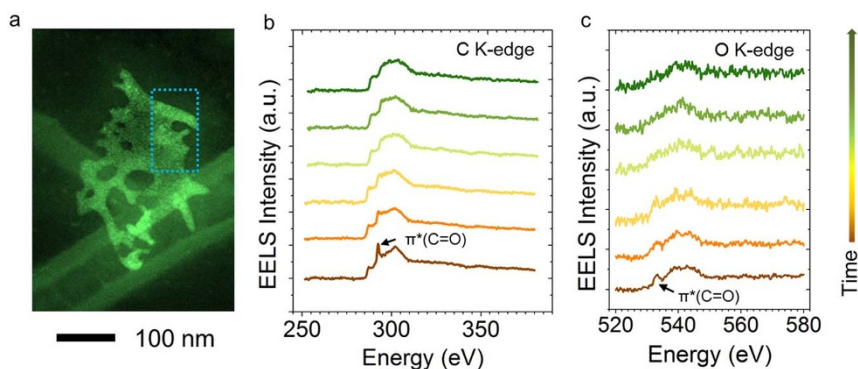


Figure 1 | Stability study of Li_2CO_3 phase on a lithiated NiO nanosheet. (a) Annular dark-field scanning transmission electron microscopy (ADF-STEM) image with an area identified for EELS acquisition. (A 200 keV electron beam (~ 12 pA) rapidly scanned the area repeatedly to spread the dose during EELS acquisition.) (b) C K-edge EELS spectra. (c) O K-edge EELS spectra. Each spectrum was integrated for 5 sec with a dose rate of 100 electrons/ $\text{\AA}^2/\text{sec}$ and an accumulated dose of 500 electrons/ \AA^2 . The critical dose limit for lithium carbonate is estimated to be approximately 750 electrons/ \AA^2 placing it in sensitivity next to biomolecules (< 200 electrons/ \AA^2 at 77 K)³². The arrow to the right of (c) indicates the increased acquisition time from the bottom to the top in (b) and (c), with an interval of 5 sec.

performed following *ex-situ* TEM procedures, and the electrochemical performance was successfully correlated to the phenomena observed using TEM. Lithium-containing compounds (e.g., electrode materials, SRLs) are easily degraded under electron beams due to the knock-on effect (i.e., atomic displacements by electron-nuclear collisions)²² and thermal effects. It is therefore, critical to distinguish these processes from those arising from the electrochemistry to ensure the correct interpretation of the experimental results.

The present work was designed to understand the effect of electron beam damage on surface reaction layers and NMC materials during data acquisition using TEM. It is shown that the chemistry and structure can be severely altered under certain circumstances, such as low scan rates. The degradation processes resemble the lattice reconstruction and chemical evolution that are caused by charge-discharge cycling⁵. It is suggested that reducing the accelerating voltage and increasing acquisition speed (e.g., performing fast EELS) are necessary to avoid the beam damage.

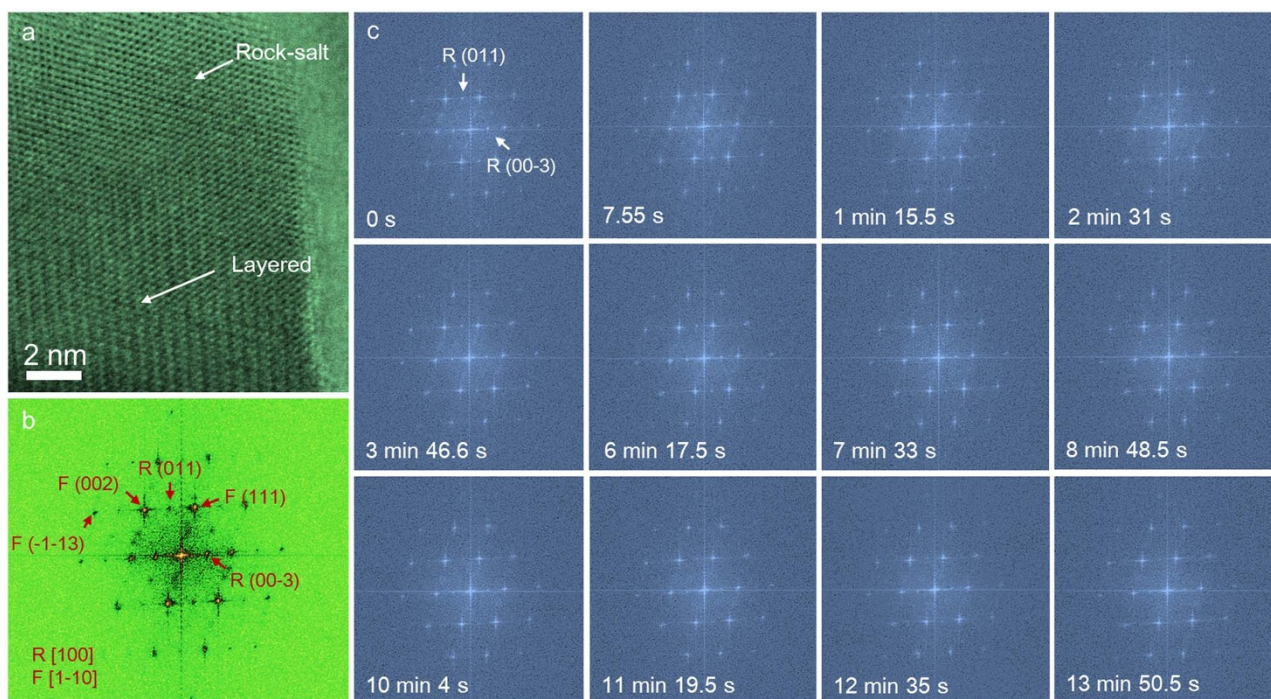


Figure 2 | Bright-field STEM (BF-STEM) observation of an NMC-based composite particle under electron beam irradiation (300 keV, ~ 36 pA, 1024×1024 pixels, pixel size 0.153 angstrom, pixel dwell time 6 μs , frame time 7.55 sec/frame). (a) BF-STEM image of an NMC particle coated with rock-salt (Fm3m) structure at the surface. (b) The corresponding fast Fourier transform (FFT) of the BF-STEM image in (a), where the zone axes for the Fm3m and $\text{R}\bar{3}\text{m}$ phases are $[1\bar{1}0]$ and $[100]$, respectively. (c) FFT results for a series of BF-STEM images under electron beam irradiation, where the FFT results correspond to pristine (0 s), 1st frame (7.55 s), 10th frame (1 min 15.5 s), 20th frame (2 min 31 s), 30th frame (3 min 46.6 s), 50th frame (6 min 17.5 s), 60th frame (7 min 33 s), 70th frame (8 min 48.5 s), 80th frame (10 min 4 s), 90th frame (11 min 19.5 s), 100th frame (12 min 35 s) and 110th frame (13 min 50.5 s) in the series. The intensity of the diffraction spots for the $\text{R}\bar{3}\text{m}$ phase decreased during exposure to the electron beam. F and R represent the Fm3m and $\text{R}\bar{3}\text{m}$ phases in the FFT indices, respectively. The corresponding BF-STEM and FFT movies are provided in Movie S1 and Movie S2 in the supplemental information, respectively.



Results

The identification of the chemical environment of SRLs (e.g., solid-electrolyte interphases) is essential to understanding their functionalities in the battery operation¹⁹. Owing to its high spatial resolution, STEM-EELS is believed to be one of the most advantageous techniques for this purpose. Carbonate groups have been shown to dominate at the surfaces of many cathode and anode materials. Figure 1 shows EELS measurements on a lithiated NiO nanosheet. In a previous study, we showed that, in NiO nanosheets, the SRLs are primarily composed of Li_2CO_3 embedded in a complex organic matrix⁶. Indeed, the fingerprints for the $1s$ to π^* transition of the CO_3^{2-} group are simultaneously observed in the C K-edge and O K-edge spectra, as shown in Figure 1b and Figure 1c, respectively. The well-defined characteristic peaks were gradually degraded after repeated EELS acquisition over the area indicated by the dashed boxed in Figure 1a, and the fine structures of the CO_3^{2-} group disappeared after four acquisitions. The compounds in the SRLs are usually prone to thermal decomposition²³. Here we showed that the combined knock-on, ionization, and thermal effects of the electron beam readily broke down the surface structure leading to the degradation of the SRL. The damage can be mitigated by acquiring EELS data from a larger area while keeping the dose below the critical limit. In addition, the critical dose limit (measured in electrons/ \AA^2) is generally dependent on the dose rate (measured in electrons/ $\text{\AA}^2/\text{sec}$). By decreasing the dose rate (i.e. reducing the incident beam current while keeping the scanning area constant), the damage rate can potentially be reduced²⁴.

A focused electron beam was scanned over a $\text{LiNi}_{0.4}\text{Mn}_{0.4}\text{Co}_{0.18}\text{Ti}_{0.02}\text{O}_2$ (abbreviated as NMC hereafter) particle that had undergone 20 electrochemical cycles between 2.0–4.7 V vs. Li^+/Li , ending in the discharged state. There are two dominant crystal structures found in the particle; $\text{R}\bar{3}\text{m}$ and $\text{Fm}\bar{3}\text{m}$ (Figure 2a). The $\text{Fm}\bar{3}\text{m}$ rock-salt structure was generated by lattice reconstruction of $\text{R}\bar{3}\text{m}$ (filling of $\text{R}\bar{3}\text{m}$ $3a$ sites by transition metals) as a result of oxygen loss and concomitant lithium ion removal during cycling^{5,21,25}. In Figure 2b, Fast Fourier transform (FFT) of the high-resolution bright-field STEM (BF-STEM) image (Figure 2a) show distinct diffraction spots for the $\text{R}\bar{3}\text{m}$ and $\text{Fm}\bar{3}\text{m}$ crystal structures along the zone axes of $\text{R}\bar{3}\text{m}[100]$ and $\text{Fm}\bar{3}\text{m}[1\bar{1}0]$, respectively. During electron beam irradiation, the $\text{R}\bar{3}\text{m}$ structure gradually converted to the $\text{Fm}\bar{3}\text{m}$ structure, as recorded in a BF-STEM mode movie (Movie S1). Selected FFT patterns shown in Figure 2c give evidence of the conversion of the $\text{R}\bar{3}\text{m}$ structure. Two characteristic diffraction spots, i.e., $\text{R}(011)$ and $\text{R}(00-3)$, are indicated in the patterns and their intensities were monitored during the irradiation process. Ultimately, after an extended irradiation period (13 min 50.5 sec, 110th frame), these two diffraction spots lost their intensities completely. The superimposed FFT patterns are presented in Movie S2.

The crystal orientation relationship between the $\text{Fm}\bar{3}\text{m}$ and $\text{R}\bar{3}\text{m}$ structures is visualized by inverse FFT imaging, as shown in Figure 3. The $\text{Fm}\bar{3}\text{m}$ (111) and $\text{R}\bar{3}\text{m}$ (003) facets are selectively visualized by masking the corresponding diffraction spots in the FFT pattern (Figures 3a and 3b, and the insets therein). The lattice spacing of the $\text{R}\bar{3}\text{m}$ (003) of the NMC phase is approximately twice as large as that of the $\text{Fm}\bar{3}\text{m}$ (111) spacing of the rock-salt phase (MO, M = Ni, Mn, Co); i.e., there is $\sim 5\%$ of mismatch, so that the rock-salt phase grew epitaxially on the layered phase. The inset of Figure 3b exemplifies the epitaxial growth of $\text{Fm}\bar{3}\text{m}$ on $\text{R}\bar{3}\text{m}$ in real space. The inverse FFT images were generated for the $\text{R}\bar{3}\text{m}/\text{Fm}\bar{3}\text{m}$ composite particle before (Figure 3c) and after (Figure 3d) electron beam damage. The initial $\text{R}\bar{3}\text{m}/\text{Fm}\bar{3}\text{m}$ composite particle (Figures 3c) was completely converted to a pure $\text{Fm}\bar{3}\text{m}$ phase after electron beam damage (Figure 3d). The phase transition process likely proceeded *via* transition metals moving from $3b$ sites to $3a$ sites, resulting in the collapse of the layered structure and the formation of a pure rock-salt structure.

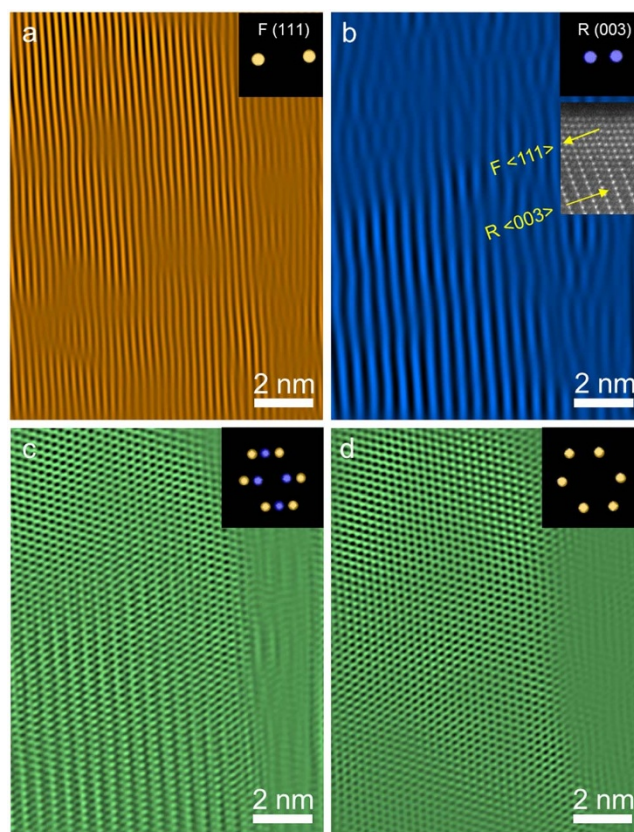


Figure 3 | Inverse FFT images of an $\text{R}\bar{3}\text{m}/\text{Fm}\bar{3}\text{m}$ composite particle obtained by placing masks on the FFT patterns. (a) Inverse FFT image of $\text{Fm}\bar{3}\text{m}$ (111) planes before electron beam irradiation. (b) Inverse FFT image of $\text{R}\bar{3}\text{m}$ (003) planes before electron beam damage, and the ADF-STEM image in the inset shows an example for the orientation relationship between the $\text{Fm}\bar{3}\text{m}$ and $\text{R}\bar{3}\text{m}$ structures. (c) Inverse FFT image of the $\text{R}\bar{3}\text{m}/\text{Fm}\bar{3}\text{m}$ composite particle before electron beam damage. (d) Inverse FFT image of the $\text{R}\bar{3}\text{m}/\text{Fm}\bar{3}\text{m}$ composite particle after electron beam irradiation. The diffraction spots masked for inverse FFT imaging are shown in the insets, where the purple and yellow spots correspond to $\text{R}\bar{3}\text{m}$ and $\text{Fm}\bar{3}\text{m}$ phases, respectively.

The requirement for simultaneous lithium and oxygen removal during the $\text{R}\bar{3}\text{m}$ -to- $\text{Fm}\bar{3}\text{m}$ transition implies that the transition metals are reduced during the process. The changes in the oxidation state of transition metals (TMs) were monitored by EELS and are shown in Figure 4. The transition metal L-edge EELS measures the dipole allowed transitions from metal $2p$ orbitals to unoccupied metal $3d$ orbitals, including both the $2p_{3/2}$ (L_3) and $2p_{1/2}$ (L_2) spin-orbit final states, and indirectly probes the local hybridization states for metal-oxygen octahedral units (i.e., TMO_6) in NMC materials^{26–28}. The O K-edge EELS corresponds to the transition from $\text{O}1s$ states to unoccupied $\text{O}2p$ states in the conduction band. Due to the $\text{TM}3d\text{-O}2p$ hybridization, O K-edge spectra also reflect the unoccupied $\text{TM}3d$ states²⁹. Although the exact nature of the hole states (e.g., location) depend on the degree of covalency in the TMO_6 octahedral unit, it is generally agreed that, in the (Ni, Mn, Co)- O_6 octahedral unit, the intensity of the pre-edge of the O K-edge is in a positive relationship with the formal oxidation states of (Ni, Mn, Co) due to the sharing of hole states in the TMO_6 unit³⁰. A continuous data acquisition mode was used to collect EELS spectra on a selected region shown in Figure 4a. As the acquisition proceeded, the electron beam gradually damaged the NMC particle. There was an incubation period from 0–40 s in the integrated pre-edge intensity before it dropped dramatically at 50 s, indicating that an accumulation of lattice interruptions by electron beam was

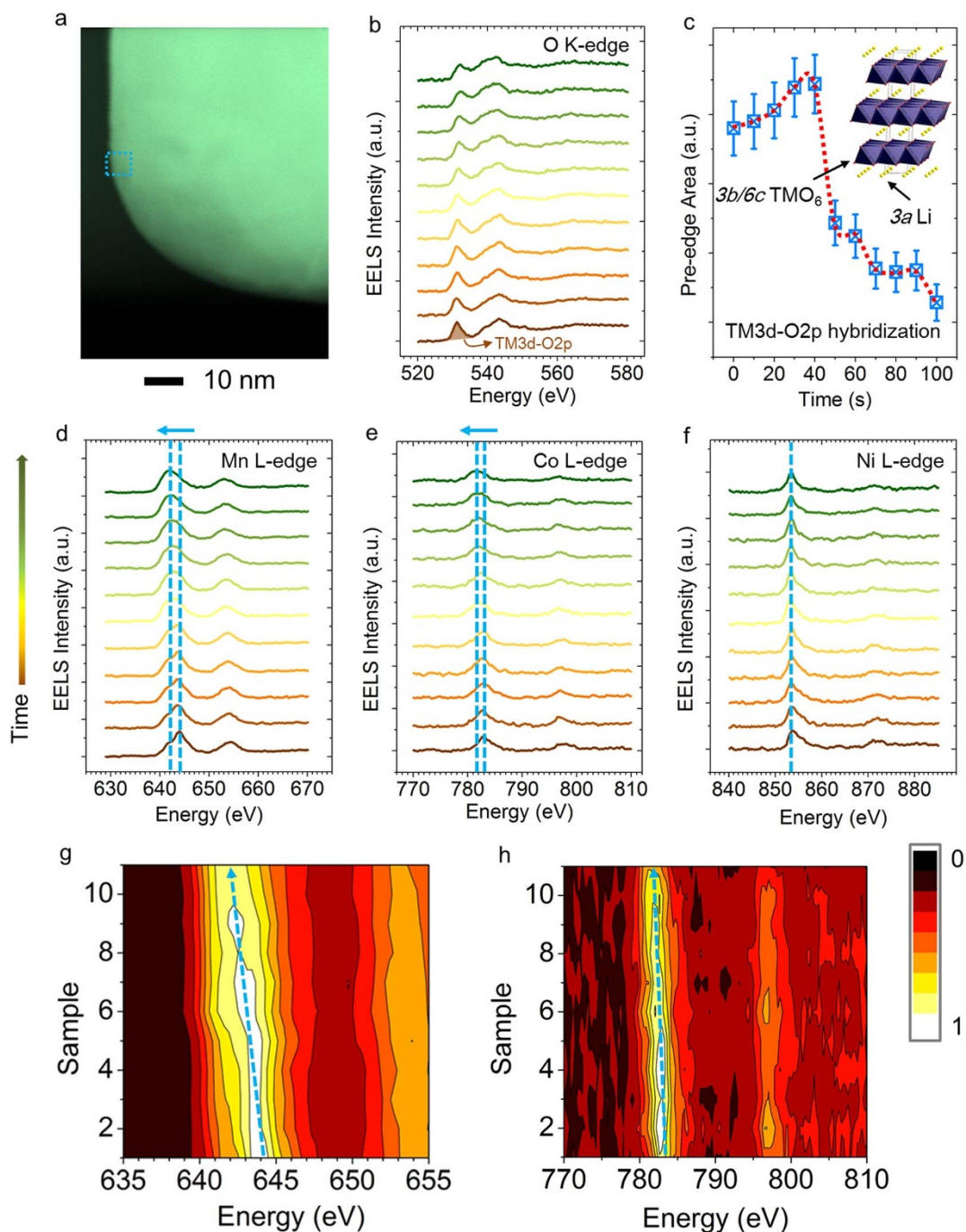


Figure 4 | EELS study of an NMC particle using a continuous acquisition mode. (a) STEM image of the particle with the selected region for EELS data collection. (b) O K-edge EELS spectra. (c) O K-edge pre-edge integrated intensity as a function of electron beam irradiation time. The pre-edge intensity corresponds to $TM3d-O2p$ hybridization states in the $3b$ sites, as shown in the inset. The integrated pre-edge intensity is in a positive relationship with the oxidation states of TMs in the TMO_6 octahedral units. (d–f) TM L-edge spectra corresponding to the O K-edge spectra in (b), where the shifts of L_3 peaks are indicated by the dashed lines and arrows. The arrow to the left of (d) indicates the increased exposure time from the bottom to the top in (d), (e) and (f), with an interval of 10 sec. (g, h) 2D EELS maps enhanced for visualization of the peak shifts for Mn (g) and Co (h). Each spectrum was integrated for 10 sec with a dose rate of 113,000 electrons/ $\text{\AA}^2/\text{sec}$ and an accumulated dose of 1,130,000 electrons/ \AA^2 . It shows that the critical dose limit for NMC material is approximately 6,000,000 electrons/ \AA^2 , which is four orders of magnitude higher than that of lithium carbonate.

necessary to initiate the removal of lithium and oxygen. TM L-edge EELS investigation provided more direct evidence for the changes in the oxidation states of transition metals, as shown in Figures 4d–h. The formal oxidation states of Ni, Mn and Co in the pristine NMC structure are +2, +4 and +3, respectively⁵. The most salient features of the TM L-edge spectra can be captured by the peak positions of TM- L_3 edges. As the acquisition proceeds (from the bottom to the

top in Figures 4d, 4e, 4g and 4h), there are noticeable peak shifts towards lower energy for Mn- L_3 and Co- L_3 edges, indicating that Mn and Co were both gradually reduced. As expected, Ni remained in the +2 oxidation state in the R3m and Fm3m structures. The synergistic changes in the oxidation states of oxygen and transition metals suggest that the hole states are shared by the transition metals and oxygen in the TMO_6 unit.

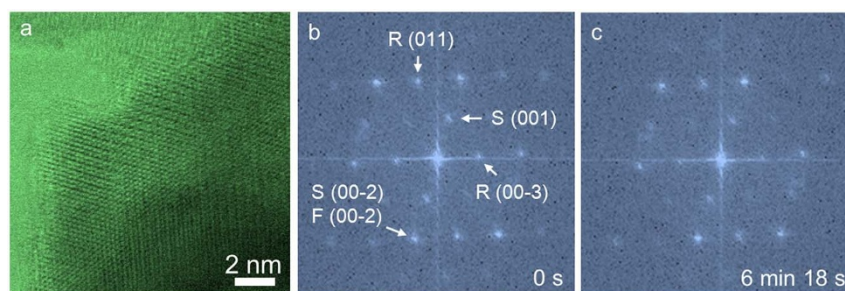


Figure 5 | BF-STEM observation of an $R\bar{3}m/Fm\bar{3}m/Fd\bar{3}m$ composite particle under electron beam with a $4\times$ faster frame rate (300 keV, ~ 36 pA, 512×512 pixels, pixel size 0.306 angstrom, pixel dwell time 6 us, frame rate 1.89 sec/frame). (a) BF-STEM image of a particle edge region with similar thickness and crystal orientation relative to that of Figure 2a. (b) FFT pattern of the composite particle before electron beam damage, where the rock-salt, spinel and layered structures are observed in the pattern. Note that the $Fd\bar{3}m$ phase is an intermediate during the $R\bar{3}m$ -to- $Fm\bar{3}m$ transition in electrochemical cycles^{5,21}. (c) FFT pattern of the composite particle after electron beam damage, which corresponds to the 200th frame (6 min 18 s) in the series. The corresponding BF-STEM movie is provided in the supplemental information (Movie S3). F, R and S represent the $Fm\bar{3}m$, $R\bar{3}m$ and $Fd\bar{3}m$ phases in the FFT indices, respectively.

Decreasing the dose rate is critical in reducing radiation damage because isolated bond breaking is healable in conductive solid samples^{24,31}. Rastering the beam over an area is an efficient way to reduce the dose rate. If the beam is idle, the dose rate is the beam current normalized by the beam area. If the beam is scanned sufficiently fast, the dose is spread out over the scanning area; in this case, the dose rate is the beam current normalized by the entire scanning area. To test how scan rate affect the dose rate, we performed a parallel experiment to compare with the condition used in Figure 2. As shown in Figure 5, we preserved the beam current, the field of view, and the dwell time but reduced the pixel number by a factor of four (i.e. scanning was four times faster). When the beam damage was compared under these two conditions after similar number of frames (i.e., similar repeat of electron beam scanning), it shows that the structural damage was significant less than that in Figure 2. In the $R\bar{3}m/Fm\bar{3}m/Fd\bar{3}m$ composite particle (Figure 5a), the $R\bar{3}m$ phase was preserved even after extended number of frames (compare Figures 5b and 5c). This suggests that ultrafast scanning in conjunction with drift correction is desirable for STEM imaging of radiation sensitive battery materials.

Discussion

We have shown that electron beam damage is a common phenomenon affecting battery materials studied by TEM. For example, the Li_2CO_3 component in the SRL of a lithiated NiO nanosheet rapidly decomposed during EELS data acquisition. NMC cathode materials also degraded at low scan rates or with intensive doses. Li K-edge EELS energy onset is buried between the M-edges of transition metals in NMC cathode materials, while transition metal oxidation states are also prone to change. These intrinsic characteristics make the direct evidence of lithium removal unlikely using Li K-edge EELS during irradiation. Nevertheless, during electron beam irradiation, the formal oxidation states of Mn and Co were reduced from +4 to +2 and from +3 to +2, respectively. Therefore, correlating the present *in situ* BF-STEM and EELS results with previous studies^{5,21}, one can determine that the degradation process involved simultaneous lithium and oxygen removal from the $3a$ and $6c$ sites of the $R\bar{3}m$ structure, and transition metals moving from the $3b$ sites to $3a$ sites, resulting in the collapse of the layered structure and ultimate conversion to a $Fm\bar{3}m$ structure. The degradation process is similar to the lattice reconstruction observed in several classes of layered cathode materials, including NMC, lithium-rich $Li(Li_yNi_xMn_xCo_{1-2x})O_2$, and lithium-rich/manganese-rich $xLi_2MnO_3 \cdot (1-x)LiMO_2$ ($M = Mn, Ni, Co, \text{etc.}$) materials. It is also likely that the electron beam reduces transition metals first due to its strongly reducing characteristics and then knocks out and/or evaporates lithium and oxygen from the NMC material, eventually

leading to transition to an $Fm\bar{3}m$ structure. Furthermore, due to the thermodynamic instability of charged NMC materials⁵, similar degradation is supposed to occur in the charged NMC particles. The present study suggests that, under some circumstances, the lattice reconstruction induced by electron beams can be used as a model system to study structural dynamics in electrochemical processes. Finally, special caution is recommended in studying battery materials to avoid indiscriminate sample degradation. This can be achieved by increasing the irradiation area and the scan rate.

Methods

Materials synthesis and battery cycling. The syntheses of NiO and $LiNi_{0.4}Mn_{0.4}Co_{0.18}Ti_{0.02}O_2$ (NMC) were performed according to previously developed protocols^{5,6}. In short, NiO was synthesized using a solvothermal method aided with an alcohol pseudo-supercritical drying technique. NMC was synthesized using a co-precipitation method followed by high-temperature annealing with LiOH. 2032 Coin cells were fabricated using composites of NiO or NMC as working electrodes and lithium metal foils as counter electrodes. The NiO working electrodes were composed of 80 wt.% active material, 10 wt.% polyvinylidene fluoride (Kureha Chemical Ind. Co. Ltd) and 10 wt.% acetylene carbon black (Denka, 50% compressed) and loadings were typically 1–2 mg/cm² of active material. To make the electrodes, these solids were mixed into N-methyl-2-pyrrolidinone and the resulting slurry cast onto copper current collectors and dried. NMC working electrodes were prepared similarly and contained 84 wt.% active material, 8 wt.% polyvinylidene fluoride, 4 wt.% acetylene carbon black and 4 wt.% SFG-6 synthetic graphite on carbon-coated aluminum current collectors, with typical active material loadings of 6–7 mg/cm². The coin cells were assembled in a helium-filled glove box using Celgard 2400 separators and 1 M LiPF₆ electrolyte in 1:2 w/w ethylene carbonate/dimethyl carbonate (Ferro Corporation). Battery testing was performed on a computer controlled VMP3 potentiostat/galvanostat (BioLogic). NiO and NMC electrodes were cycled at C/2 and C/20 rates, respectively. 1C was defined as fully discharging or charging an electrode in 1 h, corresponding to specific current densities of 718 mA/g and 280 mA/g for NiO and NMC materials, respectively.

Electron microscopy and spectroscopy. For electron microscopy and spectroscopy measurements, the electrode particles were scratched off and deposited onto TEM grids after the desired number of electrochemical cycles. A 200 keV and a 300 keV field-emission (scanning) transmission electron microscope (S/TEM) were used for *in situ* imaging and spectroscopic studies. The 200 keV microscope was operated with an imaging condition of 11 mrad, 12 pA. The 300 keV instrument was operated with 17 mrad, 36 pA. Electron energy loss spectroscopy data sets were acquired using Gatan Tridiem spectrometers.

- Nam, K.-W. *et al.* Combining In Situ Synchrotron X-Ray Diffraction and Absorption Techniques with Transmission Electron Microscopy to Study the Origin of Thermal Instability in Overcharged Cathode Materials for Lithium-Ion Batteries. *Adv. Funct. Mater.* **23**, 1047–1063 (2013).
- Thackeray, M. M. *et al.* Li_2MnO_3 -stabilized $LiMO_2$ ($M = Mn, Ni, Co$) electrodes for lithium-ion batteries. *J. Mater. Chem.* **17**, 3112 (2007).
- Batteries for Advanced Transportation Technologies, <http://batt.lbl.gov/>, (2014) Date of access: 10/06/2014.
- Department of Energy: Vehicle Technologies Office: Batteries, <http://energy.gov/eere/vehicles/vehicle-technologies-office-batteries>, (2014) Date of access: 10/06/2014.



5. Lin, F. *et al.* Surface reconstruction and chemical evolution of stoichiometric layered cathode materials for lithium-ion batteries. *Nat. Commun.* **5**, 3529 DOI: 10.1038/ncomms4529 (2014).
6. Lin, F. *et al.* Phase evolution for conversion reaction electrodes in lithium-ion batteries. *Nat. Commun.* **5**, 3358 DOI: 10.1038/ncomms4358 (2014).
7. Ebner, M., Marone, F., Stampanoni, M. & Wood, V. Visualization and Quantification of Electrochemical and Mechanical Degradation in Li Ion Batteries. *Science*. **342**, 716–720 (2013).
8. Hu, Y.-Y. *et al.* Origin of additional capacities in metal oxide lithium-ion battery electrodes. *Nat. Mater.* **12**, 1130–1136 (2013).
9. Demeaux, J. *et al.* On the limited performances of sulfone electrolytes towards the $\text{LiNi}_{0.4}\text{Mn}_{1.6}\text{O}_4$ spinel. *Phys. Chem. Chem. Phys.* **15**, 20900–20910 (2013).
10. Kam, K. C., Mehta, A., Heron, J. T. & Doeff, M. M. Electrochemical and Physical Properties of Ti-Substituted Layered Nickel Manganese Cobalt Oxide (NMC) Cathode Materials. *J. Electrochem. Soc.* **159**, A1383–A1392 (2012).
11. Conry, T. E., Mehta, A., Cabana, J. & Doeff, M. M. Structural Underpinnings of the Enhanced Cycling Stability upon Al-Substitution in $\text{LiNi}_{0.45}\text{Mn}_{0.45}\text{Co}_{0.1-y}\text{Al}_y\text{O}_2$ Positive Electrode Materials for Li-ion Batteries. *Chem. Mater.* **24**, 3307–3317 (2012).
12. Boulineau, A., Simonin, L., Colin, J.-F., Bourbon, C. & Patoux, S. First Evidence of Manganese-Nickel Segregation and Densification upon Cycling in Li-Rich Layered Oxides for Lithium Batteries. *Nano Lett.* **13**, 3857–63 (2013).
13. Xu, B., Fell, C. R., Chi, M. & Meng, Y. S. Identifying surface structural changes in layered Li-excess nickel manganese oxides in high voltage lithium ion batteries: A joint experimental and theoretical study. *Energy Environ. Sci.* **4**, 2223 (2011).
14. Huang, J. Y. *et al.* In situ observation of the electrochemical lithiation of a single SnO_2 nanowire electrode. *Science* **330**, 1515–1520 (2010).
15. McDowell, M. T. *et al.* In situ TEM of two-phase lithiation of amorphous silicon nanospheres. *Nano Lett.* **13**, 758–64 (2013).
16. Li, J. *et al.* An Artificial Solid Electrolyte Interphase Enables the Use of a $\text{LiNi}_{0.5}\text{Mn}_{1.5}\text{O}_4$ 5 V Cathode with Conventional Electrolytes. *Adv. Energy Mater.* **3**, 1275–1278 (2013).
17. Jung, Y. S. *et al.* Unexpected Improved Performance of ALD Coated LiCoO_2 /Graphite Li-Ion Batteries. *Adv. Energy Mater.* **3**, 213–219 (2013).
18. Schroder, K. W., Celio, H., Webb, L. J. & Stevenson, K. J. Examining Solid Electrolyte Interphase Formation on Crystalline Silicon Electrodes: Influence of Electrochemical Preparation and Ambient Exposure Conditions. *J. Phys. Chem. C* **116**, 19737–19747 (2012).
19. Verma, P., Maire, P. & Novák, P. A review of the features and analyses of the solid electrolyte interphase in Li-ion batteries. *Electrochim. Acta* **55**, 6332–6341 (2010).
20. Gu, M. *et al.* Formation of the spinel phase in the layered composite cathode used in Li-ion batteries. *ACS Nano* **7**, 760–7 (2013).
21. Jung, S.-K. *et al.* Understanding the Degradation Mechanisms of $\text{LiNi}_{0.5}\text{Co}_{0.2}\text{Mn}_{0.3}\text{O}_2$ Cathode Material in Lithium Ion Batteries. *Adv. Energy Mater.* **4**, 1300787 (2013).
22. Egerton, R. F., Li, P. & Malac, M. Radiation damage in the TEM and SEM. *Micron* **35**, 399–409 (2004).
23. Ota, H., Sakata, Y., Inoue, A. & Yamaguchi, S. Analysis of Vinylene Carbonate Derived SEI Layers on Graphite Anode. *J. Electrochem. Soc.* **151**, A1659 (2004).
24. Jiang, N. & Spence, J. C. H. On the dose-rate threshold of beam damage in TEM. *Ultramicroscopy* **113**, 77–82 (2012).
25. Armstrong, A. R. *et al.* Demonstrating oxygen loss and associated structural reorganization in the lithium battery cathode $\text{Li}[\text{Ni}_{0.2}\text{Li}_{0.2}\text{Mn}_{0.6}]\text{O}_2$. *J. Am. Chem. Soc.* **128**, 8694–8 (2006).
26. Lin, F. *et al.* Hole doping in Al-containing nickel oxide materials to improve electrochromic performance. *ACS Appl. Mater. Interfaces* **5**, 301–9 (2013).
27. Lin, F. *et al.* Origin of electrochromism in high-performing nanocomposite nickel oxide. *ACS Appl. Mater. Interfaces* **5**, 3643–9 (2013).
28. Van Veenendaal, M. & Sawatzky, G. Doping dependence of Ni 2p x-ray-absorption spectra of $\text{M}_x\text{Ni}_{1-x}\text{O}$ (M = Li,Na). *Phys. Rev. B* **50**, 11326–11331 (1994).
29. Soriano, L. *et al.* The electronic structure of mesoscopic NiO particles. *Chem. Phys. Lett.* **208**, 460–464 (1993).
30. Yoon, W.-S. *et al.* Investigation of the Charge Compensation Mechanism on the Electrochemically Li-Ion Deintercalated $\text{Li}_{1-x}\text{Co}_{1/3}\text{Ni}_{1/3}\text{Mn}_{1/3}\text{O}_2$ Electrode System by Combination of Soft and Hard X-ray Absorption Spectroscopy. *J. Am. Chem. Soc.* **127**, 17479–17487 (2005).
31. Mkhoyan, K., Silcox, J., Ellison, A., Ast, D. & Dieckmann, R. Full Recovery of Electron Damage in Glass at Ambient Temperatures. *Phys. Rev. Lett.* **96**, 205506 (2006).
32. Karuppasamy, M., Karimi Nejadasl, F., Vulovic, M., Koster, A. J. & Ravelli, R. B. G. Radiation damage in single-particle cryo-electron microscopy: effects of dose and dose rate. *J. Synchrotron Radiat.* **18**, 398–412 (2011).

Acknowledgments

This work was supported by the Assistant Secretary for Energy Efficiency and Renewable Energy, Office of Vehicle Technologies of the U.S. Department of Energy under Contract No. DE-AC02-05CH11231 under the Batteries for Advanced Transportation Technologies (BATT) Program. S/TEM experiments were performed at the Center for Functional Nanomaterials, Brookhaven National Laboratory, which is supported by the U.S. Department of Energy, Office of Basic Energy Sciences under Contract No. DE-AC02-98CH10886, and at National Center for Electron Microscopy (NCEM) of the Lawrence Berkeley National Laboratory (LBNL), which is supported by the U.S. Department of Energy (DOE) under Contract No. DE-AC02-05CH11231. F.L. acknowledges Prof. Ryan Richards for the help with NiO materials. The authors thank Prof. Mark Asta for fruitful discussion. H.L.X. thanks Dr. Haime Zhang for her full support and cordial advice on this project.

Author contributions

All authors participated in conceiving the work. F.L. designed, prepared the materials and performed electrochemistry with the assistance from I.M.M. H.L.X. performed electron microscopy and spectroscopy. F.L. and H.L.X. designed and analyzed the electron microscopy and spectroscopy experiments. F.L. prepared the figures and wrote the manuscript with the assistance from all authors. M.M.D. and H.L.X. participated in supervising the work. All authors reviewed the manuscript.

Additional information

Supplementary information accompanies this paper at <http://www.nature.com/scientificreports>

Competing financial interests: The authors declare no competing financial interests.

How to cite this article: Lin, F., Markus, I.M., Doeff, M.M. & Xin, H.L. Chemical and Structural Stability of Lithium-Ion Battery Electrode Materials under Electron Beam. *Sci. Rep.* **4**, 5694; DOI:10.1038/srep05694 (2014).



This work is licensed under a Creative Commons Attribution 4.0 International License. The images or other third party material in this article are included in the article's Creative Commons license, unless indicated otherwise in the credit line; if the material is not included under the Creative Commons license, users will need to obtain permission from the license holder in order to reproduce the material. To view a copy of this license, visit <http://creativecommons.org/licenses/by/4.0/>